land

MDPI

Article

New Method for Hydraulic Characterization of Variably Saturated Zone in Peatland-Dominated Permafrost Mires

Radhakrishna Bangalore Lakshmiprasad [1,*], Stephan Peth [2], Susanne K. Woche [2] and Thomas Graf [1]

[1] Institute of Fluid Mechanics and Environmental Physics in Civil Engineering, Faculty of Civil Engineering and Geodetic Science, Leibniz Universität Hannover, Appelstraße 9A, 30167 Hannover, Germany; graf@hydromech.uni-hannover.de

[2] Institute of Earth System Sciences, Section—Soil Science, Leibniz Universität Hannover, Herrenhäuser Straße 2, 30419 Hannover, Germany; peth@ifbk.uni-hannover.de (S.P.); woche@ifbk.uni-hannover.de (S.K.W.)

* Correspondence: radhakrishna@hydromech.uni-hannover.de; Tel.: +49-511-762-4786

Abstract: Modeling peatland hydraulic processes in cold regions requires defining near-surface hydraulic parameters. The current study aims to determine the soil freezing and water characteristic curve parameters for organic soils from peatland-dominated permafrost mires. The three research objectives are as follows: (i) Setting up an in situ soil freezing characteristic curve experiment by installing sensors for measuring volumetric water content and temperature in Storflaket mire, Abisko region, Sweden; (ii) Conducting laboratory evaporation experiments and inverse numerical modeling to determine soil water characteristic curve parameters and comparing three soil water characteristic curve models to the laboratory data; (iii) Deriving a relationship between soil freezing and water characteristic curves and optimizing this equation with sensor data from (i). A long-lasting in situ volumetric water content station has been successfully set up in sub-Arctic Sweden. The soil water characteristic curve experiments showed that bimodality also exists for the investigated peat soils. The optimization results of the bimodal relationship showed excellent agreement with the soil freezing cycle measurements. To the best of our knowledge, this is one of the first studies to establish and test bimodality for frozen peat soils. The estimated hydraulic parameters could be used to better simulate permafrost dynamics in peat soils.

Keywords: palsas; soil water characteristic curve; soil freezing characteristic curve; Clausius–Clapeyron equation; bimodality; numerical modeling; parameter; optimization

Citation: Lakshmiprasad, R.B.; Peth, S.; Woche, S.K.; Graf, T. New Method for Hydraulic Characterization of Variably Saturated Zone in Peatland-Dominated Permafrost Mires. *Land* **2024**, *13*, 1990. https://doi.org/10.3390/land13121990

Academic Editors: Oskars Purmalis and Marios Drosos

Received: 18 October 2024
Revised: 14 November 2024
Accepted: 18 November 2024
Published: 22 November 2024

1. Introduction

More than 25% of the land area in the Northern Hemisphere is underlain by permafrost, which is degrading due to warming at an unprecedented rate [1]. The Arctic permafrost regions store more than half of the soil carbon on Earth [2,3], and the organic matter that stores this carbon decomposes due to permafrost degradation [4].

Peatlands are one of the characteristic features of permafrost regions. Permafrost peatlands contain nearly 277 Pg of carbon, which is approximately 14% of the global soil carbon [5]. The permafrost peatlands in the Northern Hemisphere are among the first regions affected by climate change [6,7]. The Abisko region in Northern Sweden is one such unique permafrost region. The low-lying permafrost in Abisko exists due to a combined effect of mean annual air temperatures around −2 to 2 °C, peat insulation, and low precipitation [8].

The active layer is a seasonally frozen layer on top of the permafrost table. The active layer depth is an indicator of climate change in permafrost regions [9,10]. Since the 1970s, the active layer thickness has been increasing at a rate of 0.7 to 1.3 cm year^{-1}, and 81% of the permafrost sampling points have disappeared in the Abisko region [6]. It is highly unlikely that the permafrost will still exist by the end of this century [8]. The active layer depth has shown sensitivity toward soil hydraulic parameters [11,12]. Hence, accurate

estimations of the hydraulic parameters of peat are required to better understand the active layer development in permafrost peatlands.

Cryohydrogeological models are numerical models with the added capability of modeling subsurface freeze–thaw dynamics. Several modeling efforts have simulated permafrost processes [13–16]. Modeling studies have assessed the sensitivity of the active layer depth to near-surface hydraulic properties [12,17]. However, there is a deficiency in the measurements of soil hydraulic properties in cold regions [18]. Measurements of these parameters would improve the prediction of cryohydrogeological models.

Modeling the soil freeze–thaw dynamics requires the definition of the soil freezing characteristic curve (SFCC), which is the relationship between the unfrozen water content and the temperature in freezing soil [13,19]. The SFCC can be obtained by fitting empirical (power or exponential) relationships to measurements of water content and temperature [20]. Alternatively, the SFCC can be linked to the soil water characteristic curves (SWCC) [11,21].

The SWCC establishes the relationships between volumetric water content, soil water potential head, and unsaturated hydraulic conductivity. Most SWCC assumes that the pore size distribution is unimodal [22,23], an assumption valid for mineral soils. The unimodal assumption is also widely used in numerically modeling peatland processes [24,25]. However, peatlands are dominated by near-surface organic-rich soil, which has significantly different hydraulic properties than mineral soil. Organic soils are highly porous with low bulk density, and their properties depend on the composition of the inherent plant material and degree of decomposition [26] in such a way that the unimodal pore size distribution assumption is no longer valid. Accordingly, previous investigations of the SWCC of organic soil reveal bimodal pore size distributions [26–28].

The Clausius–Clapeyron (C-C) equation for freezing–thawing soils defines the relationship between pressure and temperature at the phase transition between solid ice and liquid water. The assumption is that the pore water pressure associated with negative temperatures in freezing soils can be related to pore water pressure in drying soils [21]. Therefore, the SFCC and the SWCC can be linked with the C-C equation. Because SWCC parameters are often determined, those determined parameters can be used to derive a relationship between volumetric water content and soil water potential head-dependent temperature ($\theta[h(T)]$) [29,30].

The authors in Spaans and Baker [31] investigated SFCC for fine silt in the field by installing TDR sensors. The SFCC experiments and the $\theta[h(T)]$ relationship showed good agreement at high saturation. However, the accuracy decreased rapidly as the soil dried. The authors in Watanabe et al. [29] investigated the $\theta[h(T)]$ relationship of three mineral soils (sand, loam, and silt loam). They used the C-C equation to estimate the soil water potential head of unfrozen water, based on measured temperature. During the early freezing stage, the calculated volumetric water content was underestimated compared to the measured volumetric water content [29]. The authors in Santoyo and Baser [1] collected field and laboratory data on SFCC and SWCC for mineral soils of different grain sizes and fitted the database with SFCC estimated using the traditional constrained unimodal van Genuchten–Mualem model [VGcOrg] [23]. Most of the experimental data showed good agreement with the SFCC-estimated VGcOrg model. However, it was recommended that the lab experiments be set up in accordance with the field-site conditions. To summarize, laboratory-prepared mineral soils have been investigated thoroughly, and the $\theta[h(T)]$ relationship is mainly fitted with unimodal models.

Undisturbed organic soils from peatland-dominated permafrost mires have not been tested for their hydraulic properties. Therefore, the three main research goals of the current study are as follows: (i) Set up an in situ SFCC experiment by installing sensors for measuring volumetric water content and temperature. (ii) Conduct laboratory evaporation experiments and inverse numerical modeling to determine and compare the parameters for three suitable SWCC models. (iii) Derive an $\theta[h(T)]$ relationship for the most suitable SWCC model from (ii) and fit it to the soil freezing curves from (i) using an optimization scheme.

2. Materials and Methods

The methodology section is divided into three parts (Figure 1): (i) Set up of the in situ SFCC experiment, which involves installing volumetric water content sensors and preprocessing the data to serve as input for fitting the $\theta[h(T)]$ relationship (Section 2.2). (ii) Conduct SWCC experiments by carrying out evaporation experiments with undisturbed samples taken at the field site and inverse numerical modeling to fit and compare three SWCC models (Section 2.3). (iii) Derive a suitable $\theta[h(T)]$ relationship and fit the preprocessed SFCC data using an optimization technique (Section 2.4).

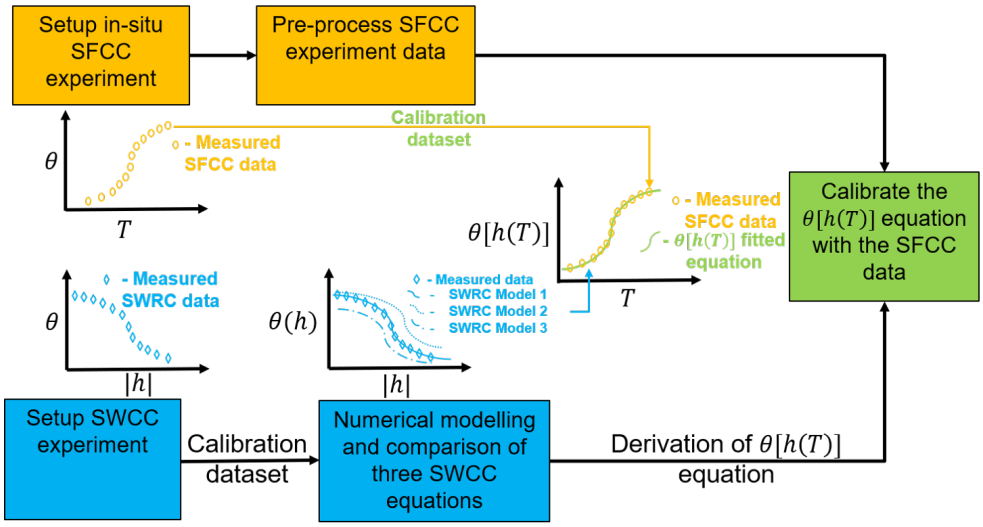

Figure 1. Schematic diagram of overall methodology: It is divided into three sections. The yellow boxes display the first section about soil freezing characteristic curve experiments. The blue boxes display the second section about conducting soil water characteristic curves (SWCC) experiments and inverse numerical modeling. The green box shows the final section about calibrating the $\theta[h(T)]$ relationship. θ, T, and h are the volumetric water content, soil temperature, and soil water potential head, respectively.

2.1. Study Area

Abisko is situated in the northernmost part of Sweden (Figure 2) and lies within the discontinuous/sporadic permafrost zone. Between 1981 and 2010, the mean annual air temperature was −0.1 °C, and the mean annual precipitation was 332 mm. The Köppen climate classification characterizes the climate in Abisko as humid subarctic with cold summers and winters. Permafrost is mainly found at elevations higher than 880 m above mean sea level and lower elevations in peat plateaus and wind-exposed ridges [8].

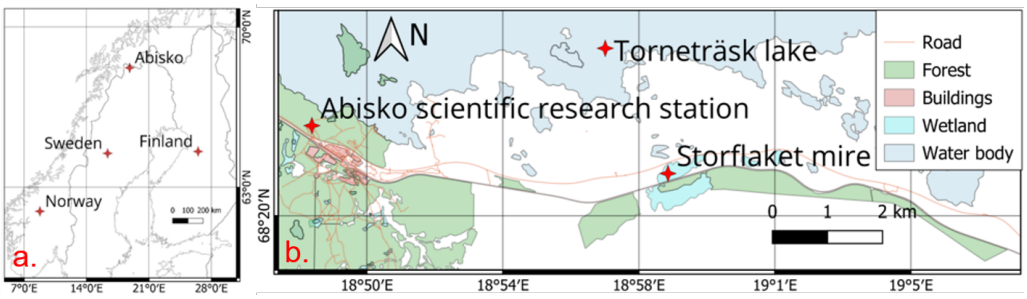

Figure 2. Study area: (**a**) Location of Abisko within Sweden. (**b**) Abisko Scientific Research Station and the Storflaket Mire are shown within the Abisko region. The land use maps and country borders were obtained from OpenStreetMap contributors [32].

Palsa mires are peat-covered mounds with a permanently frozen core commonly found in southern regions of permafrost occurrence [7]. The existence of permafrost in such palsa mires requires unique environmental conditions: mean annual air temperature below 0 °C, low precipitation rates [7], and a thick insulating organic layer. Palsas are characterized by the natural accumulation of peat layers with high organic content on the top. The topsoil of peatlands is mainly made up of slow-decomposing plant fibers such as moss, sedge, reed, and wood that have accumulated since the last glacial period [33,34]. The highly porous and lightweight peat layer can absorb large amounts of water. Hence, the water content in palsas can range from 80 to 90% by weight [35].

Storflaket mire is one of the relatively stable palsa mires in the Abisko region, with a permafrost thickness ranging from 8 to 16 m. The mire is characterized by a thick organic layer of around 0.5 m and an underlying silt layer [8]. The active layer depth was 0.5 m in dry sites and more than 1 m in wet sites [36]. The dominant vegetation varies between graminoids in wet minerotrophic conditions and dwarf shrubs in dry ombrotrophic conditions [8].

2.2. Soil Freezing Characteristic Curve (SFCC): In Situ Experiment

Figure 3 illustrates the location and depth of the twelve installed TEROS-12 sensors, purchased from METER Group GmbH, Munich, Germany (Table A1, see Appendix A.1). The sensors use capacitance technology to measure soil volumetric water content and temperature. A total of six soil profiles were considered, and two sensors were installed at each location (Figure A2). The sensors measured data every 15 min with an accuracy of ±3.0% and ±0.4 °C for volumetric water content and temperature, respectively. The sensors were installed at the end of June 2022, and the depth of the suprapermafrost groundwater table was at 0.3 m.

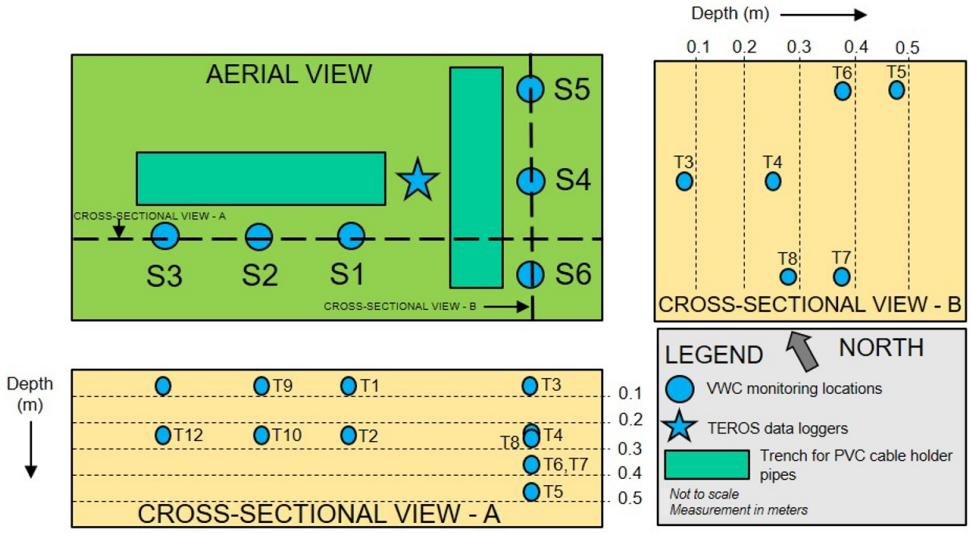

Figure 3. Schematic diagram of volumetric water content sensor installation layout: It shows the aerial and cross-sectional views. The soil profiles are labeled from S1 to S6, and the sensors are labeled from T1 to T12. Two sensors are present at each soil profile.

The volumetric water content sensor data were processed in four steps: (i) The data were reduced so that only the temperature range between −2 and 2 °C was considered because the freezing–thawing transition occurs within this temperature range. (ii) The dataset was reduced to include only the first freezing period between November and December 2022 because the entire dataset for the first freezing period was available. (iii) The $\theta[h(T)]$ relationship was established for only negative temperatures; therefore, the datasets considered only temperatures below 0 °C. (iv) The volumetric water content sensor data showed multiple values for the same temperature due to zero-curtain effect and freezing point depression. Such volumetric water content data points were

averaged to determine a single data point for a given temperature. The final preprocessed data were considered a calibration dataset for the new $\theta[h(T)]$ relationship derived in Sections 2.3 and 2.4.

2.3. Soil Water Characteristic Curves (SWCC): Laboratory Experiment and Inverse Numerical Modeling

The two SWCC consist of the soil water retention curve (SWRC) and the unsaturated hydraulic conductivity curve (HCC). The SWRC establishes the relationship between volumetric water content and soil water potential head [$\theta(h)$], while the HCC defines the relationship between unsaturated hydraulic conductivity and soil water potential head [$K(h)$]. The SWRC and HCC can be determined by evaporation experiments and inverse numerical modeling.

Evaporation experiments: The evaporation experiments were conducted with a HYPROP (Hydraulic Property) instrument (METER Group GmbH, Munich, Germany) as shown in Figure 4. Twelve soil samples were taken at the six soil profiles and two depths (0.1 m and 0.25 m) close to the soil trenches where the volumetric water content sensors were installed (Table A1 and Figure A2). The HYPROP setup is an evaporation experiment that measures soil water potential heads and volumetric water content. The hydraulic conductivity of the soil is calculated by the upward flow of a volume of water due to evaporation and the corresponding time taken for upward flow [37]. Figure 5 shows a few photos from the experiment. The experimental procedure follows the steps in the HYPROP manual [38].

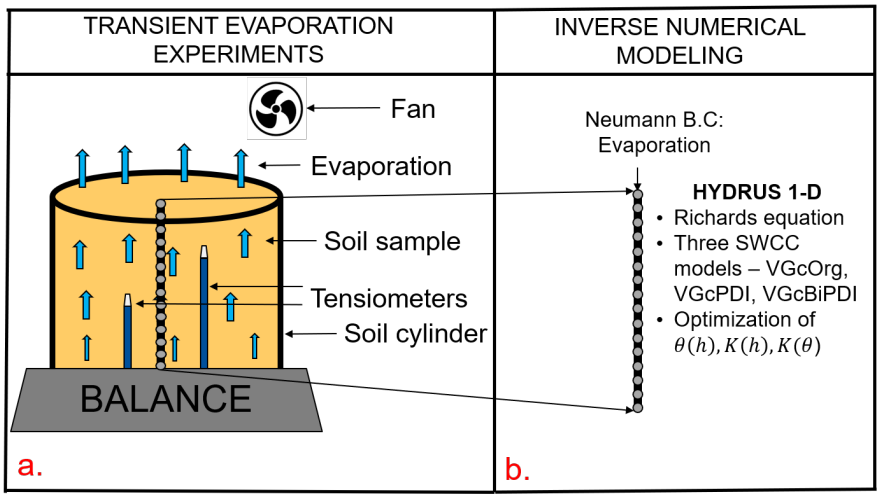

Figure 4. Conceptual diagram for determining SWCC: (**a**) A conceptual model of the evaporation experiment was set up to measure the soil water potential head and wet soil weight. (**b**) Conceptual model showing a 1D model setup that simulates the variably saturated processes in the subsurface domain due to evaporation that occurs from (**a**).

Inverse numerical modeling: The main goal of the numerical model was to simulate the transient movement of water through the subsurface domain and to calibrate three suitable SWCC models based on the measured data from the evaporation experiment. The Hydrus-1D code was used to numerically solve the Richards equation describing variably saturated flow [39,40]:

$$\frac{d\theta(h)}{dt} = \frac{d}{dz}\left[K(h)\frac{dh}{dz} + K(h)\right] \quad (1)$$

where z [L] is the vertical space coordinate (positive upwards), and t [T] is time. The 1D model was discretized by 101 equally spaced nodes. The initial condition was a fully saturated 1D column. A no-flow boundary condition was assumed at the bottom. The evaporative flux calculated from the soil weight change was applied as the top flux bound-

ary condition. The Richards equation was solved by parameterizing the relationships $\theta(h)$ [-] and $K(h)$ [L T^{-1}] [28]. The parameterization was carried out for three SWCC models.

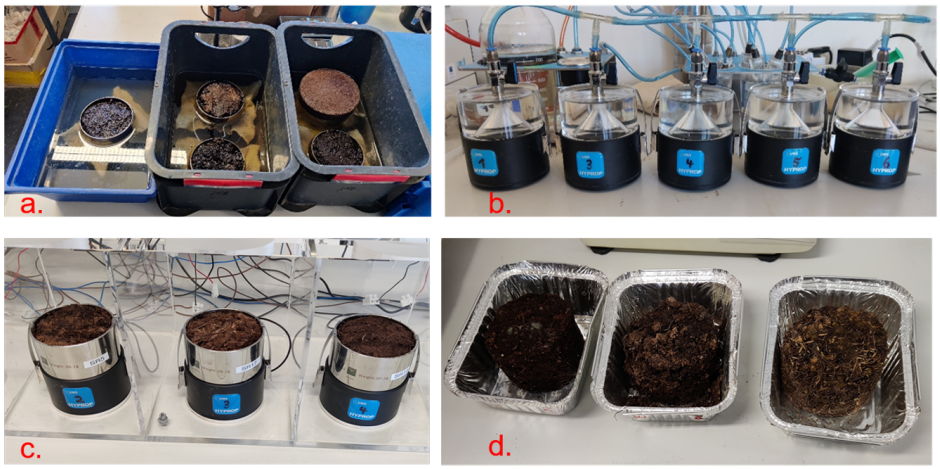

Figure 5. Photos from evaporation experiment: (**a**) Saturation of soil samples by placing a porous lid and cloth material on the bottom of the sample, placing the sample within a container, and filling water close to the brim of the soil sample. (**b**) Degassing the sensor units to remove any air bubbles. (**c**) Evaporation measurements of soil water potential head and wet soil weight. (**d**) Soil samples after oven drying to determine the dry bulk density and porosity of the soil sample.

The three chosen SWCC models were the following: (i) VGcOrg—Traditional constrained unimodal van Genuchten–Mualem model; (ii) VGcPDI—PDI-variant constrained unimodal van Genuchten–Mualem model; (iii) VGcBiPDI—PDI-variant bimodal constrained van Genuchten–Mualem model. The models were chosen to test two physical phenomena: (i) Modality or a number of pore size distributions; (ii) Non-capillary or film flow of water. The VGcOrg model considers only a single pore size distribution, and the film flow of water is assumed to be the residual water content [23]. The VGcPDI model also considers a single pore size distribution, and the film water is explicitly modeled. Additionally, the volumetric water content decreases to zero at the soil water potential head, corresponding to oven dryness [28,41]. The VGcBiPDI model considers dual pore size distribution and considers both capillary and film water [26]. The equations for VGcOrg are provided in the Appendix A.2.

The multimodal Peter–Durner–Iden Model groups (VGcPDI and VGcBiPDI) are given by the following equation [42]:

$$\theta(h) = (\theta_s - \theta_r)S_c(h) + \theta_r S_{nc}(h) \quad (2)$$

where $S_c(h)$ [-] is the saturation function of completely filled capillaries and $S_{nc}(h)$ [-] is the saturation function of non-capillary or adsorbed water. The capillary saturation function is given by [42]:

$$S_c(h) = \frac{\Gamma(h) - \Gamma_0}{1 - \Gamma_0} \quad (3)$$

where $\Gamma_0 = \Gamma(h_0)$ [-] is the value of the saturation function at the soil water potential head corresponding to oven dryness (h_0). The relative saturation function Γ is given in Equation (A2). The Γ in VGcPDI and VGcBiPDI are provided by Equation (A2) when k = 1 and k = 2, respectively. The saturation function in non-capillary water is given by [42]:

$$S_{nc}(h) = 1 + \frac{1}{x_a - x_0}(x - x_a + b \cdot \ln[1 + \exp(\frac{x_a - x}{b})]) \quad (4)$$

where x = $log_{10}(-h)$, $x_a = log_{10}(-h_a)$, $x_0 = log_{10}(-h_0)$, and $h_a = -1/\alpha$. The Equation (4) represents a linear increase in non-capillary water content vs. Log (−h) from zero at oven

dryness up to its maximum at soil water potential head h_a, from where it remains at its maximum until full saturation. The parameter b smoothens the function and renders it differentiable. The HCC function for the multimodal Peter–Durner–Iden Model groups is given in the Appendix A.3.

The total number of parameters for the VGcOrg, VGcPDI, and VGcBiPDI models is 6, 9, and 12, respectively. The parameters for each model are as follows: (i) VGcOrg—α [L^{-1}], n [-], θ_r [-], θ_s [-], K_s [$L\ T^{-1}$], τ [-]. (ii) VGcPDI—α, n, θ_r, θ_s, K_s, τ, pF_{dry} [L], ω [-], a [-]. (iii) VGcBiPDI—α_1, α_2, n_1, n_2, θ_r, θ_s, K_s, τ, pF_{dry}, ω, w_2, a.

Calibration (Inverse modeling): The optimum parameter values for the three SWCC models were estimated using inverse modeling. $\theta(h)$, $K(h)$ and $K(\theta)$ were the three curves to be fitted. The calibration data included measured volumetric water content, measured soil water potential head, and calculated hydraulic conductivity. The soil water potential head corresponding to oven dryness was taken as $h_0 = -10^{6.8}$ cm [42]. The non-capillary conductivity parameter and the soil water potential head at oven dryness were set as a = 1.5 and pF_{dry} = 6.8 [42]. The remaining parameters were allowed to vary as shown in Table 1. The parameters were estimated by minimizing a weighted-least squares objective function. The Root Mean Square Error ($RMSE$) and Akaike information criterion ($AICc$) are used to evaluate the performance of the SWCC models [38]:

$$RMSE = \sqrt{\frac{1}{r}\sum_{i=1}^{r}(y_i - \hat{y}_i)^2} \tag{5}$$

where y_i and $\hat{y}_i$ are the measured and model predicted quantities (volumetric water content or hydraulic conductivity), respectively. An increase in the number of estimated parameters for nested models may lead to a smaller value of the $RMSE$. However, the increase in the number of parameters needs to be accounted for. Therefore, $AICc$ [-] is given by

$$AICc = q \cdot ln\left(\frac{1}{q}\sum_{i=1}^{q}\left(\frac{y_i - f(t_i, \hat{p})}{\sigma_i}\right)^2\right) + 2n_p + 2\frac{n_p(n_p+1)}{q - n_p - 1} + C \tag{6}$$

where n_p is the number of estimated parameters, and q is the total number of observations. The first term penalizes a poor fit, and the second term penalizes the increase in parameters. The third term is a correction term for small values of m/n_p. More weight is provided to $\theta(h)$ compared to $K(h)$ and $K(\theta)$ due to the uncertainty associated with the estimates of K.

Table 1. Input for optimization of SWCC models: Upper and lower bounds for optimizing the parameters of the three SWCC models using the experimental data for SWCC evaporation. The three SWCC models are as follows: (i) VGcOrg—traditional constrained unimodal van Genuchten–Mualem model; (ii) VGcPDI—PDI-variant constrained unimodal van Genuchten–Mualem model; (iii) VGcBiPDI—PDI-variant bimodal constrained van Genuchten–Mualem model.

Parameters	Lower Bound	Upper Bound	Unit	Models
α, α_1	1×10^{-5}	0.5	cm^{-1}	(i), (ii), (iii)
n, n_1	1.01	15	-	(i), (ii), (iii)
θ_r	0	0.4	-	(i), (ii), (iii)
θ_s	0.1	1	-	(i), (ii), (iii)
α_2	1×10^{-5}	0.5	cm^{-1}	(iii)
n_2	1.01	15	-	(iii)
w_2	0	1	-	(iii)
K_s	0.01	10,000	cm day^{-1}	(i), (ii), (iii)
τ	-1	10	-	(i), (ii), (iii)
ω	1×10^{-9}	0.1	-	(ii), (iii)
a	-5	0	-	(ii), (iii)

2.4. Soil Water and Freezing Characteristic Curve Relationship and Optimization Procedure

$\theta[h(T)]$ relationship: The primary independent variables of SWCC [$\theta(h)$] and SFCC [$\theta(T)$] are soil water potential head and temperature, respectively. SWCC are converted to SFCC by the C-C equation, which defines the relationship between soil water potential head and temperature. The C-C equation is given by [29]:

$$h = \frac{L_f}{g} \ln\left(\frac{T}{T_m}\right) \tag{7}$$

where L_f [L^2T^{-2}] is the latent heat of fusion, g [$L\ T^{-2}$] is the acceleration due to gravity, T is the temperature, and T_m is the transition temperature. The assumption is that the soil water potential head is given by $P_{wf} = \rho_w g h$ [$M\ L^{-1}\ T^{-2}$]. The calculated value of h can be substituted in the Equation (2) of SWRC to obtain the $\theta[h(T)]$ relationship.

$$\theta[h(T)] = (\theta_s - \theta_r) S_c\left[\frac{L_f}{g} \ln\left(\frac{T}{T_m}\right)\right] + \theta_r S_{nc}\left[\frac{L_f}{g} \ln\left(\frac{T}{T_m}\right)\right] \tag{8}$$

Optimization procedure: The Equation (8) established for VGcBiPDI was used to simulate the volumetric water content based on the selected sub-zero temperatures. The simulated dataset was calibrated with the preprocessed measured dataset from the in situ SFCC experiment. The least square function from the Python 3 package scipy.optimize was used to determine the optimum parameters [43]. The trust region reflective algorithm minimizes the least squares function [44]. The residuals to be minimized were taken as input to the function. The residuals were calculated by the difference between the simulated and preprocessed measured values. The initial parameter values for the optimization scheme were taken from the results of the SWCC experiment. The lower and upper bounds for the parameters are given in Table 2. The transition temperature (T_m) was also considered an optimization parameter from the C-C equation.

Table 2. Input for optimization of $\theta[h(T)]$ relationship: Upper and lower bounds for the parameters for the least squares optimization scheme for the derived $\theta[h(T)]$ relationship.

Parameters	Lower Bound	Upper Bound	Unit
ϕ	0.92	0.98	-
α_1	0.002	0.2	cm^{-1}
n_1	1	14	-
θ_r	0	0.4	-
θ_s	0.6	0.98	-
α_2	0.0001	0.08	cm^{-1}
n_2	1	14	-
w_2	0	0.9	-
T_m	270	275	K

3. Results and Discussion

3.1. Soil Freezing Characteristic Curve (SFCC)

Figure 6 displays the soil temperature and the volumetric water content from July 2022 to November 2023 for soil profiles S1 to S3 at 0.1 m and 0.25 m below the ground surface. Figure A3 (Appendix B.1) shows the soil temperature and volumetric water content from 0.10 m to 0.50 m for soil profiles S4 to S6. The volumetric water content measurements can be divided into three periods: (i) Thawed period: It ranges from July to September. The frozen soil thaws during the summer with temperatures above 0 °C. (ii) Transition period: It can be further divided into the freezing transition period and the thawing transition period. The freezing transition period ranges from October to December, and the thawing transition period ranges from May to June. The air temperature decreases to below 0 °C during the freezing transition period, where the liquid water changes to ice. The air temperature increases to above 0 °C during the thawing transition period, where the ice changes to

liquid water. The start of the transition period is influenced by the zero-curtain effect, where temperatures remain near 0 °C for a definite period because the phase change between water and ice is retarded due to latent heat release [45]. (iii) Frozen period: It ranges from January to April when the temperatures are below 0 °C. The volumetric water content reaches its minimal value close to or at the residual water content and remains at this value for the entire period even though the temperature goes below −10 °C.

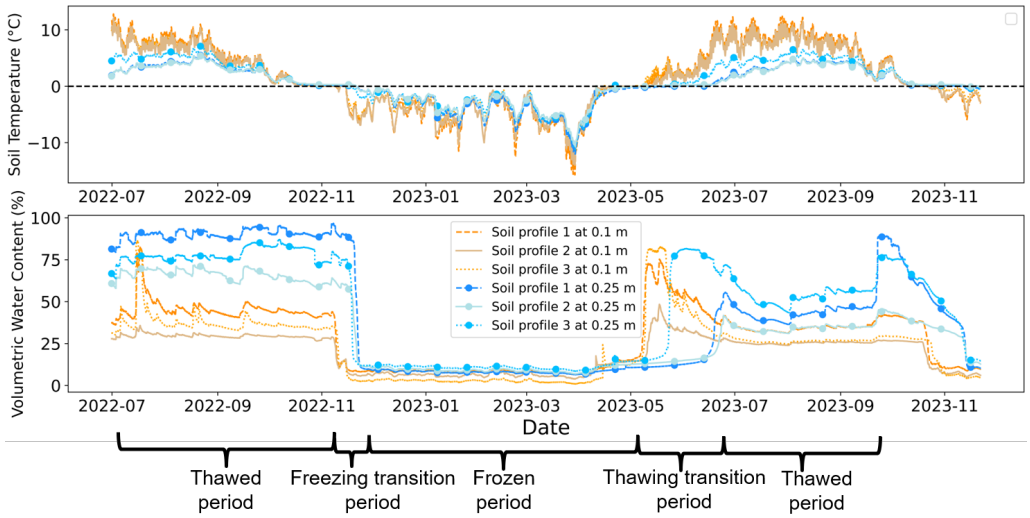

Figure 6. Results of sensor data—Part 1: Soil temperature and volumetric water content at the three soil profiles from S1 to S3 at depths 0.1 m and 0.25 m from July 2022 to November 2023. The volumetric water content periods can be divided into thawed, freezing transition, frozen, thawing transition, and thawed periods.

The mean saturated volumetric water content for sensors below 0.3 m is 85%, which is roughly the saturated water content for peat soils [28,46]. The measured mean residual water content is 6%, which could be considered a relatively low value for peat soils according to literature [28].

The SFCCs during the first freezing transition period (October to December 2022) show the characteristic sigmoidal or S-shaped curves [20] (Figure 7). The SFCCs are characterized by the following: (i) Initial water content; (ii) Transition temperature; (iii) Residual water content [19]. SFCCs for freezing curves are further analyzed because freezing curves are similar to drying curves from the evaporation experiments [21]. The initial water content prior to the transition freezing period defines the maximum volumetric water content before the volumetric water content decreases due to freezing. The transition temperature is the temperature around which the freezing or thawing processes occur (Equation (7)). The transition temperature is influenced by freezing point depression due to pore geometry and solutes. Therefore, the transition temperature is usually not identical to the melting point of pure water (0 °C) [19]. The residual water content is the unfrozen water content that remains unfrozen even at low temperatures because the water molecules are tightly bound to the soil particles. Therefore, it is energetically favorable for the water molecules to remain in the liquid state [19].

As the temperature decreases below 0 °C, the rate of decrease in volumetric water content is slower as depth increases. This means that the slope of the SFCCs is related to the transition period. The SFCC curves at 0.1 m and 0.25 m depth are relatively smooth compared to 0.3 m, 0.4 m, and 0.5 m because the volumetric water content deeper than 0.3 m is within the saturated zone and closer to the permafrost table. Therefore, they are influenced by lateral groundwater flow and cryosuction. The volumetric water content at 0.1 m and 0.25 m was applied for the $\theta[h(T)]$ analysis because SWCC measurements were only conducted at these two depths.

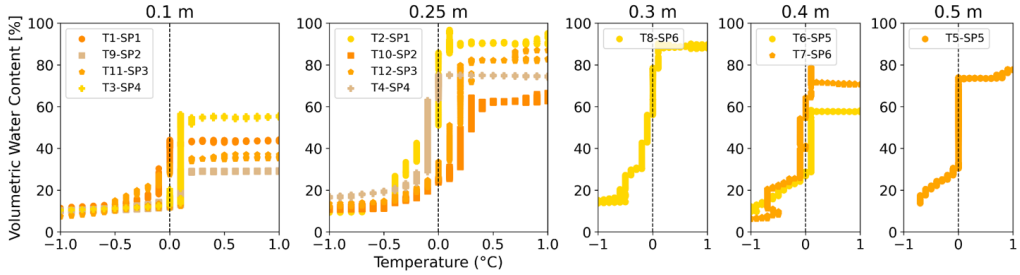

Figure 7. Pre-processed sensor data: Soil Freezing Characteristic Curves (SFCC) for the first freezing transition period (October to November 2022) at depths 0.1 m, 0.25 m, 0.3 m, 0.4 m, and 0.5 m. Only the measurements made in the −1 to 1 °C range are shown in this figure.

3.2. Soil Water Characteristic Curves (SWCC)

Soil Water Retention Curve (SWRC): The measured and simulated variables of the soil water retention curves at 0.1 m and 0.25 m are shown on the left side of Figure 8. The three soil profiles (SP1, SP2, and SP4) are shown here because they exhibited unique behavior. The results from the remaining soil profiles are shown in the Appendix B.2. The average measured volumetric water content ranges around 10 to 86% for 0.1 m and 12 to 82% for 0.25 m. The results from the SFCC experiments (Section 3.1) also show maximum volumetric water content around 80 to 90%, which is similar to literature values [46]. The maximum volumetric water content also reduces from 0.1 to 0.25 m due to a reduction in pore sizes from the self-consolidation of the soil. The measured values show a gradual decrease in volumetric water content due to evaporation with increased soil water potential head. However, the gradual reduction in the measured values shows both uni-modal and bimodal behavior. The bimodal behavior is exhibited by the sudden decrease in volumetric water content, mainly in the dry range (Figure 8). In soil profile SP1, the volumetric water content at 0.1 m is lower than 0.25 m as the soil water potential head increases. Therefore, the water holding capacity is higher at 0.25 m compared to 0.1 m. However, at SP2 and SP4, volumetric water content and soil water potential head measurements at 0.1 m and 0.25 m are similar, which could be due to the presence of thicker sphagnum moss in SP1 compared to SP2 and SP4 (Appendix A.1—Figure A2).

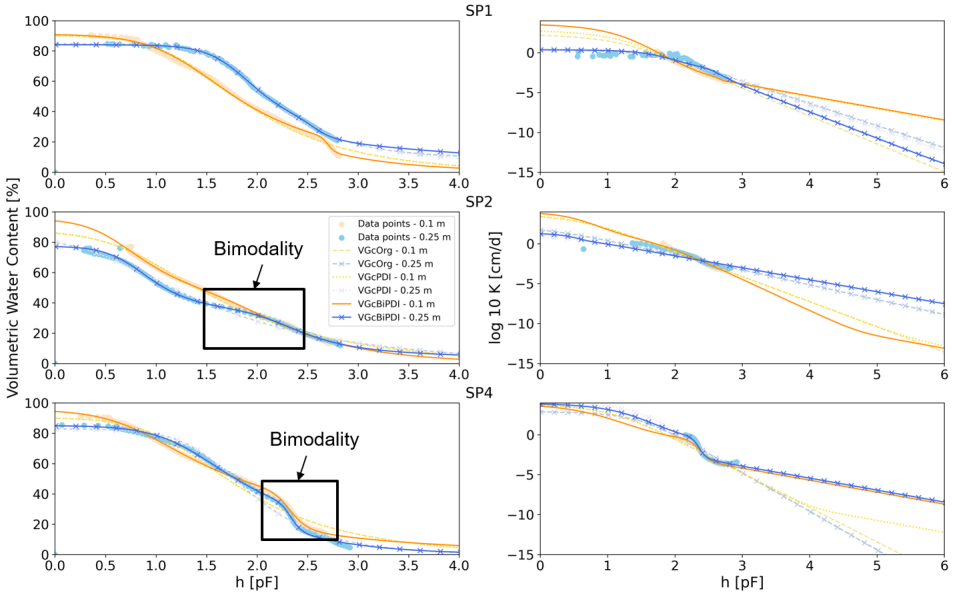

Figure 8. Results of SWCC analysis—Part 1: Measured and simulated soil water retention curves [$\theta(h)$] and hydraulic conductivity curves [$K(h)$] for soil profiles SP1, SP2, and SP4 at depths 0.1 m and 0.25 m. The simulated values are the three models that fit with the optimum parameters. The x-axis represents the soil water potential head and is displayed as pF = $log_{10}(|h|)$ where $|h|$ is in cm.

The qualitative comparison of the three model fits (VGcOrg, VGcPDI, VGcBiPDI) is explained here. The soil samples at 0.25 m for SP1 and 0.1 m for SP2 showed unimodal behavior; therefore, the VGcOrg model fits as well as the two other models to the measured data. However, the remaining samples show bimodal behavior, mainly in the dry range. The bimodality in the dry range is observed at SP4, where there is a change in the slope of the values between volumetric water content ranges of 10 to 30%. Bimodal behavior was observed in the mid-volumetric water content range (30 to 50%) by the soil sample at 0.25 m for SP2. Most soil samples showing bimodality fit better with VGcBiPDI than VGcOrg or VGcPDI. Bimodal behavior is a consequence of a change in pore size distribution. Weber et al. [47] classifies the pore spaces in living sphagnum moss to inter-, intra-, and inner-plant pore spaces. Due to pedogenesis, the inter-plant pores collapse and lead to homogeneous and bi-modal pore size distribution [47], as also observed in this study. Initially, the intra-plant pore spaces release all the water into the atmosphere, followed by the inner-plant pores spaces. The intra- and inner-plant pore spaces exhibit different SWRC, as also observed in literature [47]. No significant difference was observed between VGcOrg and VGcPDI for all soil samples. Therefore, VGcPDI does not appreciably improve the predictions by explicitly modeling the film flow of water. Weber et al. [47] also determined that the change in pore size distribution with depth influenced the SWRC. However, these effects were not prominently observed in SWRC. Similar SWCC experiments at greater depths would reveal the change in SWRC with depth but have not been conducted here.

Hydraulic Conductivity Curve (HCC): The measured and simulated variables of HCC at 0.1 m and 0.25 m are shown on the right side of Figure 8. The determined unsaturated hydraulic conductivity (K) from the measured values ranges from 0 to 10^{-5} cm day^{-1}. The measured soil water potential head values range from pF 1 to 3, except for SP4, which has a shorter measurement range from pF 2 to 3. However, the simulated K values have been projected to a greater range. K decreases with the decrease in soil water potential head because K is directly dependent on volumetric water content. As the volumetric water content reduces and the soil dries, thin films of disconnected water lead to an exponential decrease in hydraulic conductivity [48]. The change in the slope of the determined hydraulic conductivity is clearly observed for soil samples of SP4. It could indicate the bimodal behavior, which signifies the change in slope of K in accordance with the change in pore size distribution.

This paragraph explains the qualitative comparison of the three model fits for HCC. The difference in the three fits is better observed in the HCC than in the SWRC. The HCC model fits at 0.1 m and simulates a higher K compared to 0.25 m because 0.1 m is associated with higher porosity. However, this difference is not observed for soil samples at SP4, which is similar to the SWRC. The predictions in the dry range also show significant differences, although conclusions cannot be drawn about the difference at 0.1 m and 0.25 m. The difference between the three models is better observed in the wet and dry ranges. For SP1 at 0.1 m, the VGcBiPDI model predicts the highest K along with a better fit to the measured data. VGcOrg predicts the lowest K in the wet range. For SP1 at 0.25 m, the three model fits are similar in the wet range; on the other hand, the VGcBiPDI model predicts a lower K than the two other models. A minor difference exists between the three model fits for SP2. For SP4 at 0.1 m and 0.25 m, the six model fits show more or less similar predicted values in the wet range. Nevertheless, deviations are observed in the dry range. The VGcBiPDI model at both depths predicts higher K than the remaining models. Qualitatively, the VGcBiPDI model simulates the measured values better than VGcOrg and VGcPDI, especially the change in slope of K in the measured range.

Evaluation metrics for the SWCC: The quantitative comparison of the three models fits (VGcOrg, VGcPDI, VGcBiPDI) using the $RMSE$ and $AICc$ is discussed here (Figure 9 and Table A2). The first plot in the figure shows the box plot of $RMSE$ for SWRC ($\theta(h)$). The average $RMSE$ value is 0.085 for all three models, which states that all the models have a good fit with the measured values. The VGcOrg and VGcPDI models show a similar box plot; nonetheless, the VGcBiPDI model shows a higher standard deviation. The second

plot in the figure shows the box plot of $RMSE$ for HCC ($K(h)$). The average $RMSE$ value is around 0.2 to 0.4 cm day^{-1}, which implies that the performance of the models for HCC has been improved. On the other hand, more weight is provided to the SWRC compared to HCC, which could be why the $RMSE_\theta$ is lower than $RMSE_K$. The VGcBiPDI performs best, followed by the VGcPDI and VGcOrg for $RMSE_K$. The third plot shown in the figure is the $AICc$ for the three model fits. A lower $AICc$ represents a better model fit. The VGcBiPDI model also performs best compared to the other models with the least average $AICc$ value, followed by VGcOrg and VGcPDI.

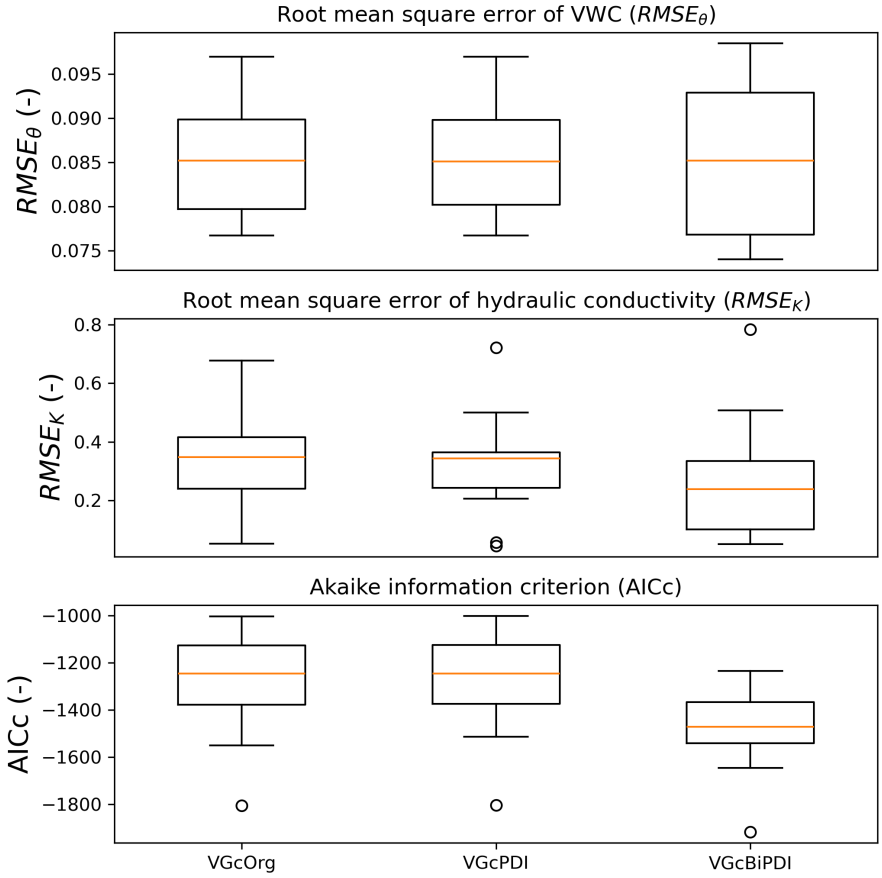

Figure 9. Results of SWCC analysis—Part 2: The box plot of $RMSE$ value of soil water retention curve (first plot—$\theta(h)$), hydraulic conductivity curve (second plot—$log_{10}K(h)$) and Akaike information criterion (third plot) for the three model fits—VGcOrg, VGcPDI, and VGcBiPDI with respect to the measured values from the SWCC experiments.

In summary, the SWRC shows relatively good fits for all three models, although the VGcBiPDI model performs significantly better in terms of $RMSE_K$ and $AICc$. This implies that the increase in the number of parameters in the VGcBiPDI model is justified as the performance is significantly better compared to VGcOrg and VGcPDI. The VGcOrg and VGcPDI models have similar $RMSE_\theta$ and $AICc$ values. While the VGcPDI model does slightly better in predicting $RMSE_K$, the VGcOrg model can be considered because it is associated with fewer parameters than the VGcPDI model.

3.3. Soil Water and Freezing Characteristic Curve Model Optimization

Figure 10 shows the preprocessed measured and simulated variables of SFCC using the optimum parameters for the four soil profiles (SP1 to SP4) and two depths (0.1 m and 0.25 m). The simulated values using the optimum parameters show an excellent fit to the measured values, resulting in an average $RMSE$ of 0.00935. The residual volumetric water content is also well captured by the $\theta[h(T)]$ relationship. Soil samples SR1, SR2, and

SR8 have a gradual change in volumetric water content where freezing point depression is prominent, and the volumetric water content reaches its minimum value (θ_r) around −0.5 °C to −0.8 °C. The remaining samples tend to freeze around 0 °C. Therefore, most of the measurements are close to the residual water content. The soil samples at 0.25 m tend to freeze faster than 0.1 m due to cryosuction. The soil sample at 0.25 m is vulnerable to freezing since it is closer to the permafrost table. Because these liquid water molecules are in contact with ice, they begin freezing faster than the liquid water at 0.1 m, followed by a quick change in soil temperature [30,46].

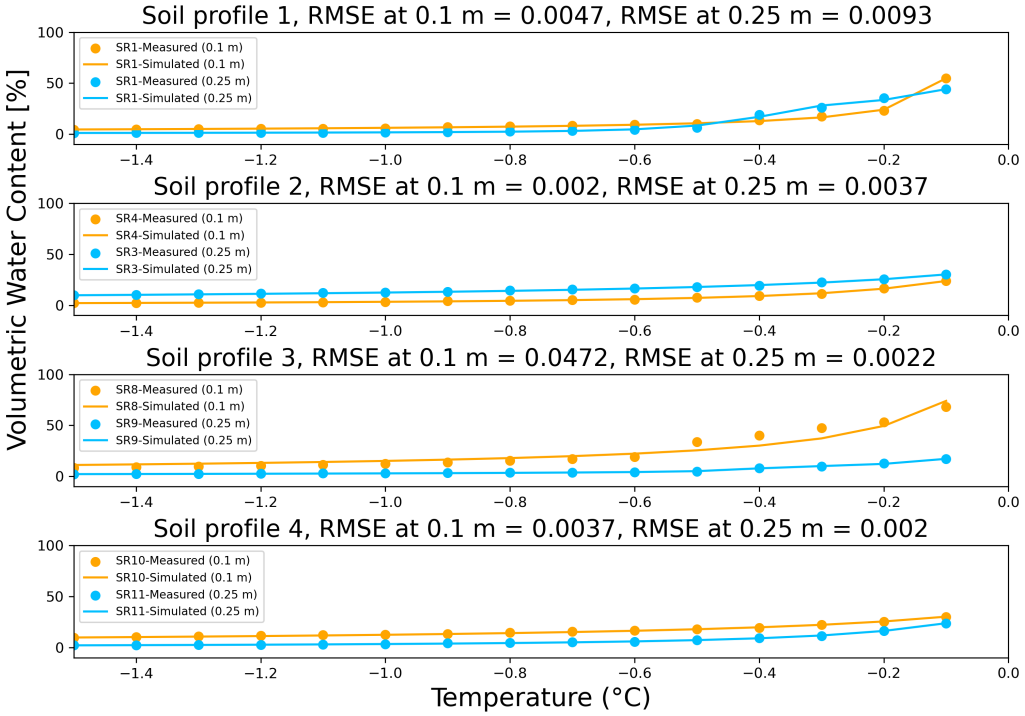

Figure 10. Optimization results of $\theta[h(T)]$ relationship: The preprocessed SFCC measured data and simulated values after optimization for the four soil profiles SP1, SP2, SP3, and SP4 at 0.1 and 0.25 m. The *RMSE* between the measured and simulated volumetric water content values are shown above each plot.

The qualitative and quantitative results from the $\theta[h(T)]$ relationship show excellent agreement with the measured data. However, the results must be cautiously assessed because of the following: (i) the SFCC and SWCC experiments were conducted in the field and lab, respectively. Although undisturbed soil samples close to the sensors were taken to ensure homogeneity between SFCC and SWCC experiments, several differences might arise when comparing the measurements. The volumetric water content sensors installed in the field are exposed to the external atmosphere, influenced by the permafrost table, lateral groundwater flow, and human or animal intervention, which could lead to discrepancies between field and lab results. Furthermore, sudden freezing and thawing can occur due to extreme weather and create disequilibrium conditions. However, the C-C equation assumes equilibrium conditions and gradual freezing of the soil [1]. (ii) the $\theta[h(T)]$ bimodal relationship is associated with nine parameters. Therefore, the results could be overfitting the measured data. The exponential increase in volumetric water content close to 0 °C could be modeled by an empirical equation with a smaller number of parameters. However, the empirical approach does not provide the relationship between SFCC and SWCC models. (iii) Ren and Vanapalli [30] highlights the importance of soil-specific calibration and careful installation of the sensors to remove any bias due to measurement errors.

4. Conclusions

The research work involved setting up an in situ SFCC experiment, conducting laboratory evaporation experiments and inverse numerical modeling, and fitting the in situ SFCC experimental data with a suitable $\theta[h(T)]$ relationship. The main results of this study are as follows:

- The volumetric water content measurements can be divided into four periods: a thawed period from July to September, a freezing transition period from October to December, a frozen period from January to April, and a thawing transition period from May to June.
- The SWCC experiments and comparison between the three SWCC models showed bimodal behavior for most of the near-surface soil samples with a thick sphagnum moss layer. The bimodal behavior was mainly observed in the dry range. Furthermore, the models that considered the contributions from film water showed only a minor improvement in results. Nonetheless, significant differences between SWCC of 0.1 m and 0.25 m were not observed.
- A new $\theta[h(T)]$ bimodal relationship has been developed for bimodal soils and calibrated with in situ SFCC experimental data. The results show excellent agreement between the measured and simulated values. The newly developed relationship can be implemented in numerical models to assess its performance in simulating hydraulic processes in permafrost peatlands.

One of the notable achievements is the successful installation of a long-lasting in situ SFCC experiment in the Storflaket mire in the Abisko region of Sweden. The volumetric water content measurements are uploaded on the online data platform SITES [49]. As far as we know, this is one of the first studies to investigate the bimodality in peatland-dominated permafrost regions by using in situ experimental data. The current study provided a methodology for improving the estimations of SFCC and SWCC near-surface properties. However, some limitations are worth noting. The volumetric water content sensors were calibrated using a general methodology recommended for peat soils by the sensor manufacturers. The general peat soil calibration method could be replaced by soil-specific calibration to improve the accuracy of the measurements. The $\theta[h(T)]$ bimodal relationship was tested in the Storflaket mire for only one freezing cycle at four locations and two depths close to the surface. The applied methodology could be tested for several freezing cycles at greater depths and in other permafrost-dominated peatland mires. Then, the temporal and spatial variations of the hydraulic parameters would provide better insights into comprehensively assessing the application of the developed methodology.

Author Contributions: R.B.L. and T.G. carried out conceptualization, formal analysis, investigation, and methodology; R.B.L., T.G. and S.P. were involved in conceptualization, methodology, and writing (reviewing and editing); T.G. and S.P. assisted in funding acquisition and supervision; R.B.L. and S.K.W. were involved in methodology, software, investigation, data curation; R.B.L. was involved in software implementation, visualization and writing (original draft). All authors have read and agreed to the published version of the manuscript.

Funding: This research is a contribution to the International Research Training Group "Geo-ecosystems in transition on the Tibetan Plateau (TransTiP)", funded by Deutsche Forschungsgemeinschaft (DFG grant 317513741/GRK 2309).

Data Availability Statement: The volumetric water content data presented in the study are openly available in Swedish Infrastructure for Ecosystem Science [SITES] at https://doi.org/10.23700/W7HX-H548. The data needs to be cited as—Lakshmiprasad, R.B., Graf, T., Rakos, N. (2024). Soil moisture, soil temperature, and electric conductivity data from Storflaket Mire, Abisko, Sweden—30 June 2022–26 October 2023 [dataset]. Swedish Infrastructure for Ecosystem Science. https://doi.org/10.23700/W7HX-H548.

Acknowledgments: We thank all the staff members of the Institute of Fluid Mechanics and Environmental Physics and the Institute of Earth System Sciences (Leibniz Universität Hannover) for their support with materials and guidance. We are grateful for the HYPROP experimental work carried out by Martin Volkmann from the Institute of Earth System Sciences. Special thanks to the TransTiP team: Nicole Börner, Andreas Hördt, Björn Riedel, Madhuri Sugund, Aida Taghavi, Raphael Schulz, Robin Zywczok, and Javiera Dörner were involved in the organization and execution of fieldwork at Abisko, Sweden. We especially thank Kaiwei Li, Kimberley Niehage, Hong Zhu and Edon Morina, for assisting with the field work and completing scientific projects to partially complete their master studies. We also appreciate the support provided by the Abisko Scientific Research Station in Sweden, mainly Niklas Rakos, Erik Lundin, Alexander Meire, and Emily Pedersen. We are grateful to Thomas Bannasch from the Institute of Dynamics and Vibration Research (Leibniz Universität Hannover) for preparing the housing box for the data loggers.

Conflicts of Interest: The authors declare no conflicts of interest.

Abbreviations

C-C	Clausius-Clapeyron
HCC	Unsaturated hydraulic conductivity curve
RC	Richards equation
SFCC	Soil freezing characteristic curves
SWRC	Soil water retention curve
VGcOrg	traditional constrained unimodal van Genuchten–Mualem model.
VGcPDI	PDI-variant constrained unimodal van Genuchten–Mualem model.
VGcBiPDI	PDI-variant Bimodal constrained van Genuchten–Mualem model

Nomenclature

Symbols	Description	Units
α_i	Shape parameter for SWRC model	L^{-1}
Γ	Effective saturation function	-
Γ_0	Saturation function for oven-dry soil water potential head	-
θ	Volumetric water content	-
$\theta_a(h)$	Air content of the soil	-
θ_r	Residual water content	-
θ_s	Saturated water content	-
ρ_{sv}	Saturated vapor density	$M\,L^{-3}$
ρ_w	Density of liquid water	$M\,L^{-3}$
τ	Shape parameter for pore tortuosity and connectivity	-
ϕ	Porosity	-
ω	Parameter describing water flow in films and corners	-
$AICc$	Akaike Information Criterion	-
a	Shape parameter for K_{rnc}	-
b	Shape parameter of saturation function for non-capillary water	-
D_a	Diffusivity of water vapor in the air	$L^2\,T^{-1}$
g	Acceleration due to gravity	$L\,T^{-2}$
h	Soil water potential head	L
h_a	Soil water potential head at residual water content	L
K	Unsaturated hydraulic conductivity	$L\,T^{-1}$
K_s	Saturated hydraulic conductivity	$L\,T^{-1}$
$K_{liq}(h)$	Volume flux of liquid water	$L\,T^{-1}$
$K_{vap}(h)$	Isothermal flux of water vapor	$L\,T^{-1}$
K_{rc}	Relative hydraulic conductivity in completely filled capillaries	-
K_{rnc}	Relative hydraulic conductivity in films and corners	-
L_f	Latent heat of fusion	$L^2\,T^{-2}$
M	Molecular weight of water	$M\,mol^{-1}$
m_i	Shape parameter for SWRC model	-

n_i	Shape parameter for SWRC model	-
n_p	Number of parameters in $AICc$	-
P_{wf}	Soil water potential	$M\,L^{-1}\,T^{-2}$
pF_{dry}	Soil water potential head at oven dryness	L
q	Total number of observations in $AICc$	-
RAW	RAW volumetric water content sensor output	-
R	Universal gas constant	$L^{-1}\,T^{-2}\,N^{-1}$
$S_c(h)$	Saturation function of completely filled capillaries	-
$S_{nc}(h)$	Saturation function of non-capillary or adsorbed water	-
T	Temperature	θ
T_m	Transition temperature	K
t	Time	day
v	Specific volume	$L^3\,M^{-1}$
v_{water}	Volume of water in the soil	L^3
v_{soil}	Total volume of the soil	L^3
w_i	Positive weights for SWRC model which sum to unity	-
z	Vertical space coordinate (positive upwards)	L

Abbreviations in nomenclature: M—Mass; L—Length; T—Time; N—Amount of substance (mol); θ—Temperature.

Appendix A. Methodology

Appendix A.1. Installation of Volumetric Water Content Sensors

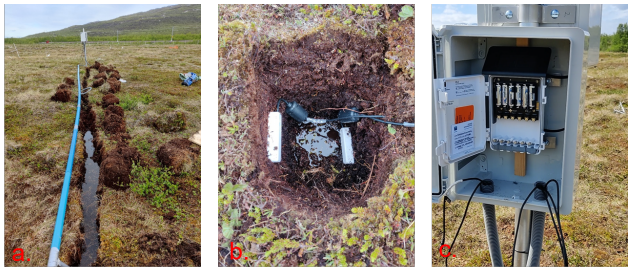

Figure A1. Fieldphotos of the volumetric water content sensor installation: (**a**) Main trench dug to install PVC pipes that contain the sensor cables. (**b**) Sensors installed at the depths of 0.1 m and 0.25 m in the soil profile SP1. (**c**) ZL6 data logger and housing box connected to the sensors.

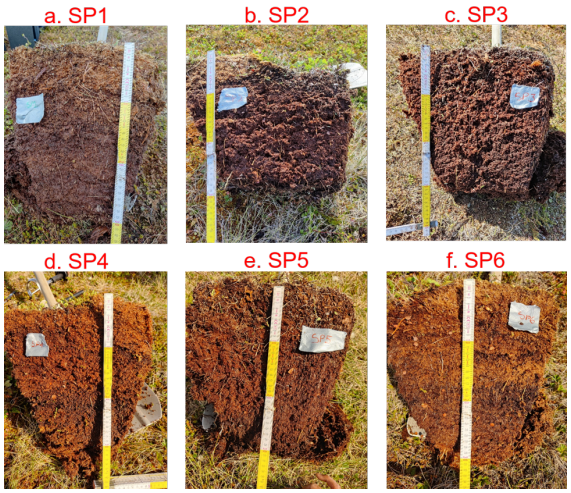

Figure A2. Photos of the six profiles from SP1 to SP6: Each soil profile had a rough dimension of 0.6 m · 0.8 m · 0.3 m (length · breadth · depth). The volumetric water content sensors were installed on the walls of the cut soil profile within the ground. Similar soil profiles were taken adjacent to these rectangular blocks to extract the soil samples for SWCC experiments.

Table A1. Locations of the twelve TEROS 12 volumetric water content sensors: The soil profile number, latitude, longitude, mean sea level, and measurement depth are provided.

TEROS 12	Soil Samples Number (Depth)	Soil Profile Number	Latitude (°N)	Longitude (°E)	Mean Sea Level (m)	Measured Depth (m)
T1	SR1 (10 cm)	SP1	68.34654189° N	18.97138583° E	381.90	0.10
T2	SR2 (25 cm)					0.25
T3	SR10 (10 cm)	SP4	68.34653223° N	18.97145605° E	381.84	0.10
T4	SR11 (25 cm)					0.25
T5	SR12 (10 cm)	SP5	68.34658900° N	18.97146969° E	381.93	0.50
T6	SR13 (25 cm)					0.40
T7	SR14 (10 cm)	SP6	68.34649929° N	18.97137513° E	381.86	0.40
T8	SR15 (25 cm)					0.30
T9	SR3 (10 cm)	SP2	68.34655665° N	18.97126332° E	382.05	0.10
T10	SR4 (25 cm)					0.25
T11	SR8 (10 cm)	SP3	68.34657068° N	18.97116002° E	381.96	0.10
T12	SR9 (25 cm)					0.25

Appendix A.2. Traditional Van Genuchten–Maulem Model

The following equations can describe the multimodal van Genuchten model group with isothermal vapor flow. The SWRC for this model group is given by the following:

$$\theta(h) = \theta_r + (\theta_s - \theta_r)\Gamma(h) \tag{A1}$$

where θ_r is the residual water content, θ_s is the saturated water content, and $\Gamma(h)$ is the effective saturation as a function of soil water potential head [50], which is given by the following:

$$\Gamma(h) = \sum_{i=1}^{k} \Gamma_i(h) = \sum_{i=1}^{k} w_i[1 + (\alpha_i h)^{n_i}]^{-m_i} \tag{A2}$$

where α_i, n_i, and m_i are shape parameters. m_i is constrained to $m_i = 1 - 1/n_i$ and w_i are positive weights which sum to unity. The unimodal VGc model is given by Equation (A2) when k = 1.

The HCC function for the multimodal van Genuchten model group accounts for both the flux of liquid water $K_{liq}(h)$ and the isothermal flux of water vapor $K_{vap}(h)$:

$$K(h) = K_{liq}(h) + K_{vap}(h) \tag{A3}$$

where $K(h)$ is the total hydraulic conductivity. The liquid hydraulic conductivity as a function of effective saturation is given by [51]:

$$K_{liq} = K_s\Gamma^{\tau}(\sum_{i=1}^{k} w_i\alpha_i)^{-2}(\sum_{i=1}^{k} w_i\alpha_i[1 - (1 - (\Gamma_i)^{1/m_i})^{m_i}])^2 \tag{A4}$$

where K_s is the saturated hydraulic conductivity and τ is a shape parameter describing pore tortuosity and connectivity. $\Gamma(h)$ is represented as Γ here.

The isothermal vapor conductivity is given by [52]:

$$K_{vap}(h) = \frac{\rho_{sv}}{\rho_w} D_a \frac{\theta_a(h)^{10/3}}{\phi^2} \frac{Mg}{RT} \exp(\frac{Mgh}{RT}) \tag{A5}$$

where ρ_{sv} is the saturated vapor density, ρ_w is the density of liquid water, D_a is the diffusivity of water vapor in air, ϕ is porosity, which is equal to θ_s, $\theta_a(h)$ represents the air content of the substrate which is the difference between ϕ and $\theta(h)$, M is the molecular weight of water, g is the gravitational acceleration, R is the universal gas constant and T is

the absolute temperature. The assumption is that the total water potential head equals the soil water potential head because organic media have low salt content [28].

Appendix A.3. Hydraulic Conductivity Curve Function for Peter–Durner–Iden Model

The HCC function for the multimodal Peter–Durner–Iden Model groups is given by [48]

$$K_{liq}(h) = (1-\omega)K_s K_{rc}(S_c) + \omega K_s K_{rnc}(S_{nc}) \quad \text{(A6)}$$

where ω is the parameter describing the relative proportion of water flow in films and corners, K_{rc} is relative hydraulic conductivity caused by flow in completely filled capillaries, and K_{rnc} is relative hydraulic conductivity caused by flow in films and corners in completely filled capillaries. K_{rc} and K_{rnc} is given by

$$K_{rc}(S_c) = S_c^{\tau}[1 - (\frac{(\sum_{i=1}^{k} w_i \alpha_i [1 - (1 - (\Gamma_i)^{1/m_i})^{m_i}])}{(\sum_{i=1}^{k} w_i \alpha_i [1 - (1 - (\Gamma_{i,0})^{1/m_i})^{m_i}])})^{m}]^2 \quad \text{(A7)}$$

$$K_{rnc}(S_{nc}) = (\frac{h_0}{h_a})^{a(1-S_{nc})} \quad \text{(A8)}$$

where $\Gamma_{i,0} = \Gamma_i(h_0)$ and Γ_i is defined according the soil water potential head defined in Equation (A2). Parameter a is set to 1.5 as suggested by Tokunaga [53] for ideally and closely packed monodisperse spheres because there are no specialized conceptual models for sphagnum moss and peat.

Appendix B. Results and Discussion

Appendix B.1. Volumetric Water Content from the Second Data Logger

The volumetric water content sensors from 0.1 to 0.5 m (Figure A3) also show relatively constant values of volumetric water content during the first thawed (2022) and frozen period (2022–2023). The second thawed period is associated with significant variability of volumetric water content, possibly due to the dry summer in 2023. The increase in temperature could have resulted in higher evaporation and lower volumetric water content in the soil profile. A similar phenomenon is observed in Figure 6. The transition period increases as the depth increases due to the effect of surface fluxes and the increase in volumetric water content. The near-surface volumetric water content is first exposed to the surface energy fluxes. Therefore, they freeze first, followed by volumetric water content at greater depths. The volumetric water content increases with depth until the permafrost table; thus, they require more latent heat energy for the phase change.

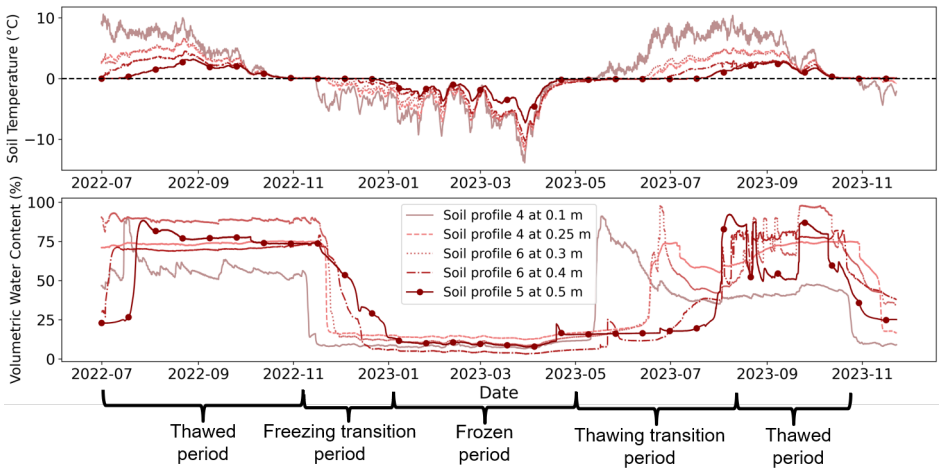

Figure A3. Results of sensor data—Part 2: Soil temperature and volumetric water content at the three soil profiles (SP4, SP5, and SP6) from depths 0.1 m to 0.5 m. The volumetric water content measurements can be divided into thawed, transition, and frozen periods.

Appendix B.2. SWCC Experiments

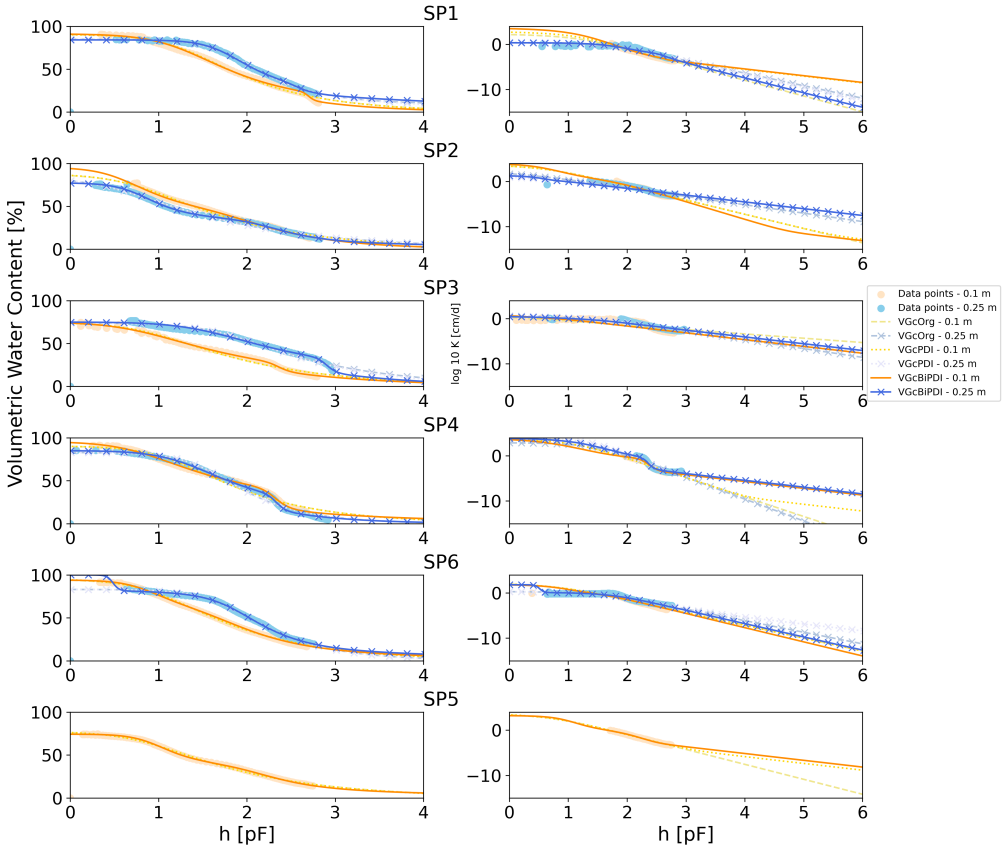

Figure A4. All sample results of SWCC analysis: Measured and simulated soil water retention curves [$\theta(h)$] and hydraulic conductivity curves [$K(h)$] for soil profiles SP1 to SP6 at depths 0.1 m and 0.25 m. The simulated values are the three model fits with optimum parameters—VGcOrg, VGcPDI, and VGcBiPDI. The x-axis is displayed as pF = $log_{10}(|h|)$ where $|h|$ is in cm.

Table A2. Evaluation statistics of SWCC analysis: Statistics of the 11 soil samples considering the $RMSE$ of $\theta(h)$, $RMSE$ of $K(h)$ and $K(\theta)$, and Akaike information criterion ($AICc$).

Soil Sample	Soil Profile	Depth (m)	Model Name	$RMSE_\theta$	$RMSE_K$	$AICc$
SR1	SP1	0.1	VGcOrg	0.0924	0.1104	−1254
SR1	SP1	0.1	VGcPDI	0.0924	0.0561	−1255
SR1	SP1	0.1	VGcBiPDI	0.0911	0.0567	−1471
SR4	SP2	0.1	VGcOrg	0.0867	0.2003	−1124
SR4	SP2	0.1	VGcPDI	0.0869	0.2065	−1124
SR4	SP2	0.1	VGcBiPDI	0.0924	0.1326	−1296
SR8	SP3	0.1	VGcOrg	0.0771	0.6769	−1450
SR8	SP3	0.1	VGcPDI	0.0769	0.7213	−1438
SR8	SP3	0.1	VGcBiPDI	0.0742	0.783	−1508
SR10	SP4	0.1	VGcOrg	0.097	0.3567	−1003
SR10	SP4	0.1	VGcPDI	0.097	0.3585	−1001
SR10	SP4	0.1	VGcBiPDI	0.0938	0.0708	−1505
SR12	SP5	0.1	VGcOrg	0.0767	0.053	−1245
SR12	SP5	0.1	VGcPDI	0.0767	0.0456	−1245
SR12	SP5	0.1	VGcBiPDI	0.074	0.0506	−1646
SR14	SP6	0.1	VGcOrg	0.0937	0.3484	−1305
SR14	SP6	0.1	VGcPDI	0.0941	0.3499	−1309
SR14	SP6	0.1	VGcBiPDI	0.0934	0.3193	−1435
SR2	SP1	0.25	VGcOrg	0.0852	0.3629	−1550
SR2	SP1	0.25	VGcPDI	0.0851	0.3432	−1514

Table A2. *Cont.*

Soil Sample	Soil Profile	Depth (m)	Model Name	$RMSE_\theta$	$RMSE_K$	$AICc$
SR2	SP1	0.25	VGcBiPDI	0.0842	0.3353	−1574
SR3	SP2	0.25	VGcOrg	0.0815	0.4697	−1130
SR3	SP2	0.25	VGcPDI	0.0816	0.5002	−1125
SR3	SP2	0.25	VGcBiPDI	0.077	0.5074	−1235
SR9	SP3	0.25	VGcOrg	0.0779	0.3001	−1200
SR9	SP3	0.25	VGcPDI	0.0788	0.291	−1159
SR9	SP3	0.25	VGcBiPDI	0.0766	0.3321	−1301
SR11	SP4	0.25	VGcOrg	0.0873	0.4984	−1089
SR11	SP4	0.25	VGcPDI	0.0872	0.3687	−1096
SR11	SP4	0.25	VGcBiPDI	0.0852	0.136	−1433
SR15	SP6	0.25	VGcOrg	0.0838	0.2793	−1805
SR15	SP6	0.25	VGcPDI	0.0838	0.2802	−1803
SR15	SP6	0.25	VGcBiPDI	0.0985	0.2388	−1917

Table A3. Optimized parameters of VGc model after inverse numerical modeling of SWCC experiments: The described statistics (mean, std—standard deviation, min—minimum, max—maximum) are calculated from all the SWCC soil samples.

		α [1/cm]	n	θ_r	θ_s	K_s [cm/Day]	τ
10 cms	mean	0.105	1.414	0	0.859	4932.265	0.305
	std	0.043	0.0540	0	0.079	5244.123	2.718
	min	0.049	1.364	0	0.747	4.99	−4.853
	max	0.164	1.491	0	0.948	10,000	3.023
25 cms	mean	0.081	1.578	0.019	0.817	259.832	−0.976
	std	0.138	0.212	0.040	0.044	384.084	1.705
	min	0.015	1.316	0	0.74	2.22	−2.443
	max	0.327	1.78	0.092	0.848	865.4	1.869

Table A4. Optimized parameters of VGcPDI model after inverse numerical modeling of SWCC experiments: The described statistics (mean, std—standard deviation, min—minimum, max—maximum) are calculated from all the SWCC soil samples.

		α [1/cm]	n	θ_r	θ_s	K_s [cm/Day]	τ	pF_{dry}	ω
10 cms	mean	0.106	1.409	0	0.860	5177.05	3.044	6.8	0.016
	std	0.045	0.054	0	0.082	5289.866	3.572	0	0.041
	min	0.049	1.358	0	0.744	10.4	−0.029	6.8	1×10^{-9}
	max	0.169	1.488	0	0.953	10,000	10	6.8	0.1
25 cms	mean	0.083	1.588	0.028	0.817	2014.066	2.202	6.8	0.024
	std	0.143	0.219	0.063	0.045	4464.337	4.836	0	0.042
	min	0.0152	1.306	0	0.737	2.27	−1	6.8	9.77×10^{-9}
	max	0.339	1.815	0.141	0.848	10,000	10	6.8	0.1

Table A5. Optimized parameters of VGcBiPDI model after inverse numerical modeling of SWCC experiments: The described statistics (mean, std—standard deviation, min—minimum, max—maximum) are calculated from the results of the SWCC experiments.

		θ_r	θ_s	K_s [cm/Day]	τ	α_1 [1/cm]	n_1	pF_{dry}	α_2 [1/cm]	n_2	w_2	ω
10 cms	mean	0.051	0.876	4430.65	3.278	0.075	3.328	6.8	0.082	3.629	0.508	0.016
	std	0.055	0.100	4653.126	3.669	0.096	2.178	0	0.080	4.643	0.273	0.041
	min	0	0.743	15.3	−0.271	0.005	1.532	6.8	0.002	1.35	0.1	1×10^{-9}
	max	0.11	0.956	10,000	10	0.2523	6.574	6.8	0.167	13.077	0.876	0.1
25 cms	mean	0.100	0.843	2018.672	2.445	0.047	3.3184	6.8	0.078	6.031	0.353	0.040
	std	0.100	0.098	4461.772	4.589	0.069	2.972	0	0.143	4.7035	0.269	0.055
	min	0	0.75	2.2	−1	0.005	1.395	6.8	0.001	1.613	0.137	1×10^{-9}
	max	0.227	0.96	10,000	10	0.169	8.589	6.8	0.331	12.95	0.804	0.1

References

1. Santoyo, S.F.; Baser, T. A review of the existing data on soil-freezing experiments and assessment of soil-freezing curves derived from soil–water retention curves. *J. Cold Reg. Eng.* **2022**, *36*, 04021020. [CrossRef]
2. Hugelius, G.; Strauss, J.; Zubrzycki, S.; Harden, J.W.; Schuur, E.A.G.; Ping, C.L.; Schirrmeister, L.; Grosse, G.; Michaelson, G.J.; Koven, C.D.; et al. Estimated stocks of circumpolar permafrost carbon with quantified uncertainty ranges and identified data gaps. *Biogeosciences* **2014**, *11*, 6573–6593. [CrossRef]
3. Ping, C.L.; Michaelson, G.J.; Jorgenson, M.T.; Kimble, J.M.; Epstein, H.; Romanovsky, V.E.; Walker, D.A. High stocks of soil organic carbon in the North American Arctic region. *Nat. Geosci.* **2008**, *1*, 615–619. [CrossRef]
4. Schuur, E.A.; Bockheim, J.; Canadell, J.G.; Euskirchen, E.; Field, C.B.; Goryachkin, S.V.; Hagemann, S.; Kuhry, P.; Lafleur, P.M.; Lee, H.; et al. Vulnerability of permafrost carbon to climate change: Implications for the global carbon cycle. *BioScience* **2008**, *58*, 701–714. [CrossRef]
5. Swindles, G.T.; Morris, P.J.; Mullan, D.; Watson, E.J.; Turner, T.E.; Roland, T.P.; Amesbury, M.J.; Kokfelt, U.; Schoning, K.; Pratte, S.; et al. The long-term fate of permafrost peatlands under rapid climate warming. *Sci. Rep.* **2015**, *5*, 17951. [CrossRef]
6. Åkerman, H.J.; Johansson, M. Thawing permafrost and thicker active layers in sub-arctic Sweden. *Permafr. Periglac. Process.* **2008**, *19*, 279–292. [CrossRef]
7. Seppälä, M. Synthesis of studies of palsa formation underlining the importance of local environmental and physical characteristics. *Quat. Res.* **2011**, *75*, 366–370. [CrossRef]
8. Johansson, M.; Akerman, J.; Keuper, F.; Christensen, T.R.; Lantuit, H.; Callaghan, T.V. Past and present permafrost temperatures in the Abisko area: redrilling of boreholes. *Ambio* **2011**, *40*, 558–565. [CrossRef]
9. Hinzman, L.; Kane, D.; Gieck, R.; Everett, K. Hydrologic and thermal properties of the active layer in the Alaskan Arctic. *Cold Reg. Sci. Technol.* **1991**, *19*, 95–110. [CrossRef]
10. Overduin, P.P.; Kane, D.L.; van Loon, W. Measuring thermal conductivity in freezing and thawing soil using the soil temperature response to heating. *Cold Reg. Sci. Technol.* **2006**, *45*, 8–22. [CrossRef]
11. Ebel, B.A.; Koch, J.C.; Walvoord, M.A. Soil Physical, Hydraulic, and Thermal Properties in Interior Alaska, USA: Implications for Hydrologic Response to Thawing Permafrost Conditions. *Water Resour. Res.* **2019**, *55*, 4427–4447. [CrossRef]
12. Zipper, S.C.; Lamontagne-Hallé, P.; McKenzie, J.M.; Rocha, A.V. Groundwater controls on postfire permafrost thaw: Water and energy balance effects. *J. Geophys. Res. Earth Surf.* **2018**, *123*, 2677–2694. [CrossRef]
13. McKenzie, J.M.; Voss, C.I.; Siegel, D.I. Groundwater flow with energy transport and water–ice phase change: Numerical simulations, benchmarks, and application to freezing in peat bogs. *Adv. Water Resour.* **2007**, *30*, 966–983. [CrossRef]
14. Stone, L.E.; Fang, X.; Haynes, K.M.; Helbig, M.; Pomeroy, J.W.; Sonnentag, O.; Quinton, W.L. Modelling the effects of permafrost loss on discharge from a wetland-dominated, discontinuous permafrost basin. *Hydrol. Process.* **2019**, *33*, 2607–2626. [CrossRef]
15. Chaudhary, N.; Westermann, S.; Lamba, S.; Shurpali, N.; Sannel, A.B.K.; Schurgers, G.; Miller, P.A.; Smith, B. Modelling past and future peatland carbon dynamics across the pan-Arctic. *Glob. Chang. Biol.* **2020**, *26*, 4119–4133. [CrossRef]
16. Dagenais, S.; Molson, J.; Lemieux, J.M.; Fortier, R.; Therrien, R. Coupled cryo-hydrogeological modelling of permafrost dynamics near Umiujaq (Nunavik, Canada). *Hydrogeol. J.* **2020**, *28*, 887–904. [CrossRef]
17. Lamontagne-Hallé, P.; McKenzie, J.M.; Kurylyk, B.L.; Zipper, S.C. Changing groundwater discharge dynamics in permafrost regions. *Environ. Res. Lett.* **2018**, *13*, 084017. [CrossRef]
18. O'Connor, M.T.; Cardenas, M.B.; Ferencz, S.B.; Wu, Y.; Neilson, B.T.; Chen, J.; Kling, G.W. Empirical Models for Predicting Water and Heat Flow Properties of Permafrost Soils. *Geophys. Res. Lett.* **2020**, *47*, e2020GL087646. [CrossRef]
19. Devoie, É.G.; Gruber, S.; McKenzie, J.M. A repository of measured soil freezing characteristic curves: 1921 to 2021. *Earth Syst. Sci. Data* **2022**, *14*, 3365–3377. [CrossRef]
20. Pardo Lara, R.; Berg, A.A.; Warland, J.; Tetlock, E. In Situ Estimates of Freezing/Melting Point Depression in Agricultural Soils Using Permittivity and Temperature Measurements. *Water Resour. Res.* **2020**, *56*, e2019WR026020. [CrossRef]
21. Kurylyk, B.L.; Watanabe, K. The mathematical representation of freezing and thawing processes in variably-saturated, non-deformable soils. *Adv. Water Resour.* **2013**, *60*, 160–177. [CrossRef]
22. Mualem, Y. A new model for predicting the hydraulic conductivity of unsaturated porous media. *Water Resour. Res.* **1976**, *12*, 513–522. [CrossRef]
23. Van Genuchten, M.T. A closed-form equation for predicting the hydraulic conductivity of unsaturated soils. *Soil Sci. Soc. Am. J.* **1980**, *44*, 892–898. [CrossRef]
24. Wu, Y.; Blodau, C. PEATBOG: A biogeochemical model for analyzing coupled carbon and nitrogen dynamics in northern peatlands. *Geosci. Model Dev.* **2013**, *6*, 1173–1207. [CrossRef]
25. Mezbahuddin, M.; Grant, R.F.; Flanagan, L.B. Modeling hydrological controls on variations in peat water content, water table depth, and surface energy exchange of a boreal western Canadian fen peatland. *J. Geophys. Res. Biogeosci.* **2016**, *121*, 2216–2242. [CrossRef]
26. Dettmann, U.; Bechtold, M.; Viohl, T.; Piayda, A.; Sokolowsky, L.; Tiemeyer, B. Evaporation experiments for the determination of hydraulic properties of peat and other organic soils: An evaluation of methods based on a large dataset. *J. Hydrol.* **2019**, *575*, 933–944. [CrossRef]
27. Quinton, W.L.; Hayashi, M.; Carey, S.K. Peat hydraulic conductivity in cold regions and its relation to pore size and geometry. *Hydrol. Process.* **2008**, *22*, 2829–2837. [CrossRef]

28. Weber, T.K.D.; Iden, S.C.; Durner, W. Unsaturated hydraulic properties of Sphagnum moss and peat reveal trimodal pore-size distributions. *Water Resour. Res.* **2017**, *53*, 415–434. [CrossRef]
29. Watanabe, K.; Kito, T.; Wake, T.; Sakai, M. Freezing experiments on unsaturated sand, loam and silt loam. *Ann. Glaciol.* **2011**, *52*, 37–43. [CrossRef]
30. Ren, J.; Vanapalli, S.K. Comparison of soil-freezing and soil-water characteristic curves of two Canadian soils. *Vadose Zone J.* **2019**, *18*, 1–14. [CrossRef]
31. Spaans, E.J.; Baker, J.M. The soil freezing characteristic: Its measurement and similarity to the soil moisture characteristic. *Soil Sci. Soc. Am. J.* **1996**, *60*, 13–19. [CrossRef]
32. OpenStreetMap. OpenStreetMap Contributions. 2023. Available online: www.openstreetmap.org (accessed on 5 June 2023).
33. Carey, S.K.; Quinton, W.L.; Goeller, N.T. Field and laboratory estimates of pore size properties and hydraulic characteristics for subarctic organic soils. *Hydrol. Process.* **2007**, *21*, 2560–2571. [CrossRef]
34. Gnatowski, T.; Szatyłowicz, J.; Brandyk, T.; Kechavarzi, C. Hydraulic properties of fen peat soils in Poland. *Geoderma* **2010**, *154*, 188–195. [CrossRef]
35. Alewell, C.; Giesler, R.; Klaminder, J.; Leifeld, J.; Rollog, M. Stable carbon isotopes as indicators for environmental change in palsa peats. *Biogeosciences* **2011**, *8*, 1769–1778. [CrossRef]
36. Dobiński, W. Geophysical characteristics of permafrost in the Abisko area, northern Sweden. *Pol. Polar Res.* **2010**, *31*, 141–158. [CrossRef]
37. Shokrana, M.S.B.; Ghane, E. Measurement of soil water characteristic curve using HYPROP2. *MethodsX* **2020**, *7*, 100840. [CrossRef]
38. Meter Group GmbH. *HYPROP Manual*; Meter Group GmbH: Munich, Germany, 2023.
39. Šimůnek, J.; van Genuchten, M.T. Modeling nonequilibrium flow and transport processes using HYDRUS. *Vadose Zone J.* **2008**, *7*, 782–797. [CrossRef]
40. Šimůnek, J.; Van Genuchten, M.T.; Šejna, M. Recent developments and applications of the HYDRUS computer software packages. *Vadose Zone J.* **2016**, *15*, vzj2016-04. [CrossRef]
41. Peters, A.; Durner, W. Simplified evaporation method for determining soil hydraulic properties. *J. Hydrol.* **2008**, *356*, 147–162. [CrossRef]
42. Iden, S.C.; Durner, W. Comment on "Simple consistent models for water retention and hydraulic conductivity in the complete moisture range" by A. Peters. *Water Resour. Res.* **2014**, *50*, 7530–7534. [CrossRef]
43. SciPy. Scipy.Optimize.Least_Squares. Available online: https://docs.scipy.org/doc/scipy/reference/generated/scipy.optimize.least_squares.html (accessed on 8 November 2023).
44. Byrd, R.H.; Schnabel, R.B.; Shultz, G.A. Approximate solution of the trust region problem by minimization over two-dimensional subspaces. *Math. Program.* **1988**, *40*, 247–263. [CrossRef]
45. Jiang, Y.; Zhuang, Q.; O'Donnell, J.A. Modeling thermal dynamics of active layer soils and near–surface permafrost using a fully coupled water and heat transport model. *J. Geophys. Res. Atmos.* **2012**, *117*, D11110. [CrossRef]
46. Kujala, K.; Seppälä, M.; Holappa, T. Physical properties of peat and palsa formation. *Cold Reg. Sci. Technol.* **2008**, *52*, 408–414. [CrossRef]
47. Weber, T.K.D.; Iden, S.C.; Durner, W. A pore-size classification for peat bogs derived from unsaturated hydraulic properties. *Hydrol. Earth Syst. Sci.* **2017**, *21*, 6185–6200. [CrossRef]
48. Peters, A. Simple consistent models for water retention and hydraulic conductivity in the complete moisture range. *Water Resour. Res.* **2013**, *49*, 6765–6780. [CrossRef]
49. Lakshmiprasad, R.; Graf, T.; Rakos, N. *Soil Moisture, Soil Temperature, and Electric Conductivity Data from Storflaket Mire*; 30 June 2022–26 October 2023; Abisko Scientific Research Station: Abisko, Sweden, 2024. 548 [CrossRef]
50. Durner, W. Hydraulic conductivity estimation for soils with heterogeneous pore structure. *Water Resour. Res.* **1994**, *30*, 211–223. [CrossRef]
51. Priesack, E.; Durner, W. Closed-form expression for the multi-modal unsaturated conductivity function. *Vadose Zone J.* **2006**, *5*, 121–124. [CrossRef]
52. Saito, H.; Simunek, J.; Mohanty, B.P. Numerical analysis of coupled water, vapor, and heat transport in the vadose zone. *Vadose Zone J.* **2006**, *5*, 784–800. [CrossRef]
53. Tokunaga, T.K. Hydraulic properties of adsorbed water films in unsaturated porous media. *Water Resour. Res.* **2009**, *45*, W06415. [CrossRef]